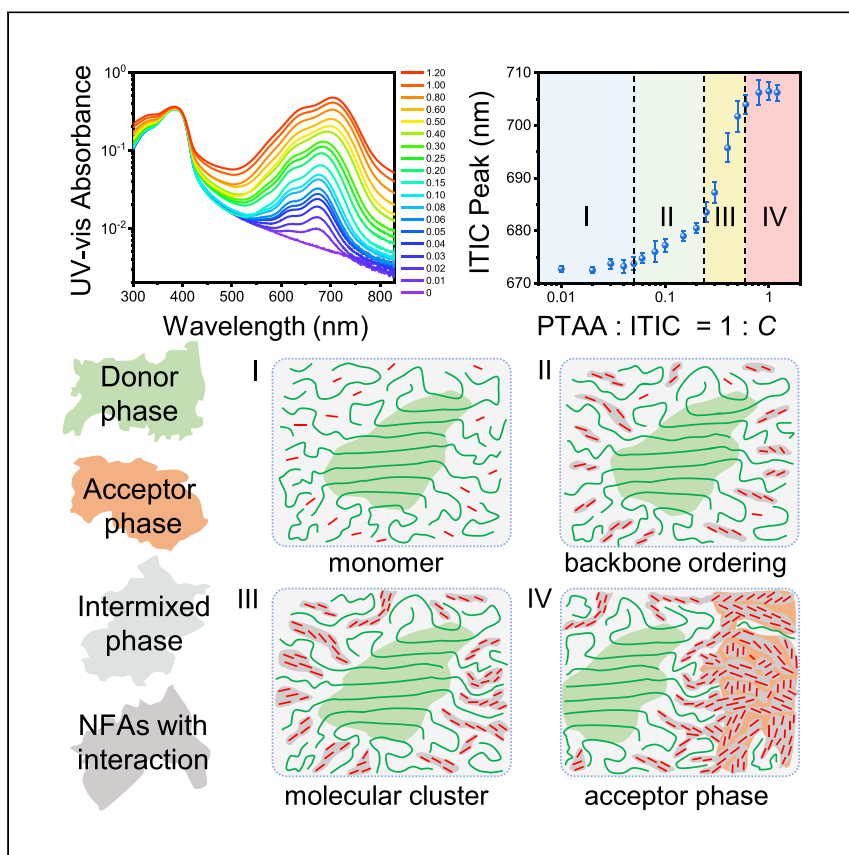


Article

Revealing aggregation of non-fullerene acceptors in intermixed phase by ultraviolet-visible absorption spectroscopy



Jin Fang, Zhen Wang, Yiyao Chen, ..., Zhixiang Wei, Harald Ade, Chang-Qi Ma

jfang2020@sinano.ac.cn (J.F.)
weizx@nanoctr.cn (Z.W.)
hwade@ncsu.edu (H.A.)
cqma2011@sinano.ac.cn (C.-Q.M.)

Highlights

Concentration-dependent UV-vis spectra reveal NFA aggregation in blend film

NFA composition in the intermixed phase is determined even at a non-equilibrium state

Molecular interactions develop between NFA molecules in the intermixed phase

The disordered intermixed phase that determines organic photovoltaic performance is difficult to probe. Fang et al. report that concentration-dependent UV-vis absorption spectra reveal NFA aggregation and composition in the intermixed phase, which is correlated with solar device performance.

Fang et al., Cell Reports Physical Science 3, 100983
July 20, 2022 © 2022 The Author(s).
<https://doi.org/10.1016/j.xcrp.2022.100983>



Article

Revealing aggregation of non-fullerene acceptors in intermixed phase by ultraviolet-visible absorption spectroscopy

Jin Fang,^{1,*} Zhen Wang,² Yiyao Chen,³ Qing Zhang,³ Jianqi Zhang,⁴ Lingyun Zhu,⁴ Maojie Zhang,⁵ Zheng Cui,¹ Zhixiang Wei,^{4,*} Harald Ade,^{2,*} and Chang-Qi Ma^{1,6,*}

SUMMARY

Non-fullerene acceptor (NFA) aggregation is crucial in determining bulk-heterojunction (BHJ) organic photovoltaic (OPV) performance. However, it is still a big challenge to characterize the nanostructure of NFAs in the disordered donor-acceptor intermixed phase. Here, we demonstrate a method to characterize NFA aggregation and composition in the intermixed phase by measuring NFA concentration-dependent ultraviolet-visible (UV-vis) absorption spectroscopy of BHJ films. In various polymer:NFA films, an absorption shift as a function of increasing molecular concentration (ASIMC) phenomenon is observed, and different NFA aggregation behaviors can be distinguished. The ASIMC method was then applied to study the influence of processing conditions on the NFA concentration in the intermixed phase of devices to establish a correlation with device efficiency. The current work provides a feasible tool to study the nanostructure of NFAs in the complex polymer matrix and to understand the variations in the NFA concentration in the intermixed phase under non-equilibrium conditions.

INTRODUCTION

Thanks to the development of small-molecule non-fullerene acceptors (NFAs) and wide-band-gap polymer donors, significant progress has been achieved in bulk-heterojunction organic photovoltaics (BHJ-OPVs).^{1–3} Power conversion efficiencies (PCEs) of single-junction devices have surpassed 19%.^{4–6} In addition to the donor and acceptor materials, of critical importance to high-performance OPVs is the molecular packing/order, composition, and morphology of the BHJ film, which is typically in a non-equilibrium state.^{7,8} BHJ morphologies result from the multi-interaction of thermodynamics and kinetics processes, including molecular interactions between donor and acceptor molecules, solution and additive properties, speed of film formation, and post-treatments.^{7,9–11} In general, the nanostructure of the BHJ is believed to be a three-phase morphology composed of a donor phase, an acceptor phase, and a disordered donor/acceptor intermixed phase.^{12–14} However, the nanostructure within the intermixed phase, including aggregate structures and compositions, is not fully understood owing to the lack of characterization methods.

At the molecular level, the intermixed phase consists of well-mixed disordered polymer donor and dispersed NFAs, where photogenerated excitons dissociate and form free charges, which diffuse through the disordered polymer and dispersed NFAs to their respective phases.^{15,16} The simulations and experimental results have revealed that an efficient charge transport channel in the NFA aggregation is

¹i-Lab & Printable Electronics Research Center, Suzhou Institute of Nano-Tech and Nano-Bionics, Chinese Academy of Sciences (CAS), Suzhou 215123, China

²Department of Physics and Organic and Carbon Electronics Laboratories (ORaCEL), North Carolina State University, Raleigh, NC 27695, USA

³Vacuum Interconnected Nanotech Workstation (Nano-X), Suzhou Institute of Nano-Tech and Nano-Bionics, Chinese Academy of Sciences (CAS), Suzhou 215123, China

⁴CAS Key Laboratory of Nanosystem and Hierarchical Fabrication, CAS Center for Excellence in Nanoscience, National Center for Nanoscience and Technology, Beijing 100190, China

⁵Laboratory of Advanced Optoelectronic Materials, College of Chemistry, Chemical Engineering and Materials Science, Soochow University, Suzhou 215123, China

⁶Lead contact

*Correspondence: jfang2020@sinano.ac.cn (J.F.), weizx@nanoctr.cn (Z.W.), hwade@ncsu.edu (H.A.), cqma2011@sinano.ac.cn (C.-Q.M.)

<https://doi.org/10.1016/j.xcrp.2022.100983>



through the end-cap π - π stacking.^{17,18} Nevertheless, knowledge about charge transport channels between dispersed NFAs in the intermixed phase is still limited.

The acceptor's composition in the intermixed phase has been suggested to affect the efficiency and stability of BHJ-OPV by influencing charge transport and recombination.^{13,19} From the point of view of thermodynamics, the equilibrium composition of the acceptors in the intermixed phase is dependent on the molecular interaction between the donor and the acceptor, an interaction that can be captured by the Flory-Huggins interaction parameter.^{13,20} However, the thermodynamic equilibrium state is not easy to achieve for BHJ films.⁷ Moreover, in most cases, there is a gap between the thermodynamic equilibrium state and the morphology-optimized state that results in devices with high PCEs. Because of this, the acceptor composition needs to be adjusted to the percolation threshold.²¹ As part of the non-equilibrium nature of the optimized morphology, small-molecule acceptors immiscible in the donor material within the intermixed phase tend to diffuse out of the percolation threshold as aging occurs.^{22–24} At times, device performance first increases as the percolation threshold is crossed during diffusion-driven purification.²² Although the influence of the intermixed phase composition has been well delineated in the literature,¹³ systematic research on the composition evolution in the intermixed phase of NFA-based OPVs after the solution coating, post-treatment, and aging processes is still lacking. This is primarily because the intermixed phase lies between the donor and the acceptor phases, and it is spatially too small to be directly observed. Moreover, the composition in the intermixed phase is statistical.^{25,26}

Up to now, several methods have been reported to estimate the thermodynamic interactions and composition of the intermixed phase, i.e., time-of-flight secondary ion mass spectrometry (TOF-SIMS),²⁷ scanning transmission X-ray microscopy (STXM),^{14,28} visible light microscopy (VLM),²⁹ grazing-incidence wide-angle X-ray scattering (GIWAXS),³⁰ small-angle neutron scattering (SANS),^{31,32} and resonant soft X-ray scattering (R-SoXS).^{16,28} TOF-SIMS, STXM, and VLM are based on the acceptors' diffusion. Thus, only the film in thermal equilibrium can be studied. GIWAXS, SANS, and R-SoXS are based on the different scattering intensities between donors and acceptors.^{30,33} However, in NFA-based OPV films, it is at times difficult but not impossible to study the composition of the intermixed phase, due to the low scattering intensity contrast between donors and acceptors.²¹ Moreover, most of these methods require advanced equipment, e.g., SIMS and synchrotron radiation X-ray, and analysis expertise, preventing widespread adoption by most of the community. Thus, developing an easily accessible and straightforward method to study the intermixed phases, especially for films in non-equilibrium states, is highly needed for a better understanding of the correlation between device performance and optical aggregation of the intermixed phase.

In this work, we present a method to quantitatively analyze the acceptor aggregation structure in the intermixed phase by measuring the UV-visible (UV-vis) absorption spectroscopy of blend films with different concentrations of NFAs. We also determine morphological and molecular packing parameters to infer the composition of the intermixed phase of NFA-based OPVs. We discover four stages in the red shift of UV-vis spectra of 2,2'-[6,6,12,12-tetrakis(4-hexylphenyl)-6,12-dihydrodithieno[2,3-d:2',3'-d']-sindacen[1,2-b:5,6-b'dithiophene-2,8-diyl]bis[methyldiyne(3-oxo-1H-indene-2,1(3H)-diylidene)]bispropanedinitrile (ITIC)¹ in a poly[bis(4-phenyl)(2,4,6-trimethylphenyl)amine] (PTAA)³⁴ matrix (see Figure S1 for the chemical structures of ITIC and PTAA) as a function of ITIC concentration. Considering also the GIWAXS results, we assign these four stages to (1) dispersed monomer at a low concentration of NFAs, (2) NFAs forming chain-like backbone ordering, (3) molecular clusters at a

mediate concentration, and (4) pure acceptor phases at a higher concentration. The absorption shift as a function of increasing molecular concentration (ASIMC) method can also be applied to analyze the nanostructure of ITIC derivatives and Y6 (molecular structures are also presented in Figure S1) on complex OPV multiphase BHJs. Finally, we use this method to study the PM7:C8-IT-4F and PM6:Y6 blend films based on OPVs prepared under different solution process conditions and with different post-treatments. A correlation of the photovoltaic performance with concentration-dependent molecular packing and aggregation is then observed. We demonstrate that the method based on UV-vis absorption spectroscopy may be a powerful tool to understand the intermixed phase and thus help to improve the photovoltaic performance of OPVs.

RESULTS

Dependence of molecular aggregation on NFA concentration

UV-vis absorption spectroscopy is one of the most effective and commonly used measurements to study the intramolecular and intermolecular optical interactions of conjugated materials.^{35–37} In the acceptor-donor-acceptor (A-D-A) configuration, small-molecule NFAs benefit from strong intramolecular interactions. These NFAs tend to possess a high absorption coefficient and narrow band gap. A red shift of dozens of nanometers is often observed when the NFA molecules are in aggregated states (for example, in the neat film), compared with monomer states (such as in dilute solution).^{1,2} In this study, we chose ITIC, one of the most widely studied NFAs, as the model conjugated small molecule for its intensive intermolecular interaction in thin solid films ($\lambda_{\text{abs}}^{\text{max}}$ shifts from 678 nm in chloroform solution to 705 nm in thin solid film; Figure 1A). Meanwhile, PTAA, a polymer with an absorption band over 300–430 nm with a $\lambda_{\text{abs}}^{\text{max}}$ of 384 nm, was chosen as the polymer matrix to offer a spectral window to study the evaluation of ITIC aggregation processes in the blend film.

In the research of self-assembled functional dyes in solutions, solutions with at least two orders of the magnitude concentration range of solute are required.^{35,38} Therefore, PTAA:ITIC weight ratios in blend films ranging from 1:0.01 to more than 1:1 were used to study the ITIC aggregated states by UV-vis absorption spectra. The list of PTAA:ITIC weight ratios and the corresponding ITIC concentrations in blend films are presented in Table S1. For convenience, we used the concentration of ITIC in PTAA to label the blend films with different weight ratios. Thus, PTAA and ITIC were regarded as solvent and solute, respectively. For example, when the PTAA:ITIC weight ratio is 1:0.01, the concentration of ITIC in PTAA is 0.01. Figure 1B depicts the evolution of the absorption spectra of the blend films with different concentrations of ITIC in PTAA. To show the variation of the ITIC absorption band more clearly, the absorbance (y axis) is presented on a logarithmic scale. The absorption band of PTAA does not change too much, which indicates that the amount of PTAA in the blend films is nearly constant, while the absorption band of ITIC (over 550–750 nm) red shifts with the increase in ITIC concentration. The normalized absorption of ITIC after subtracting the PTAA background is presented in Figure 1C. As shown in Figures 1B and 1C, the UV-vis spectra of the blend films present the phenomenon of the absorption shifting as a function of the increase in molecular concentration (ASIMC). The main (0-0) and shoulder (0-1) peaks of ITIC in solid films red shift with the rise in ITIC concentration. Figure 1D shows the evolution of the average $\lambda_{\text{abs}}^{\text{max}}$ of ITIC as a function of ITIC concentration in PTAA with error bars (films spin-coated at 1,000 rpm). Four stages could be observed for the variation of ITIC main peak versus ITIC concentration logarithm, distinguished by various colors in Figure 1D. The comparison of the $\lambda_{\text{abs}}^{\text{max}}$ versus ITIC concentration of PTAA:ITIC blend films spin-coated at 1,000 and 2,000 rpm deposited on poly(styrene

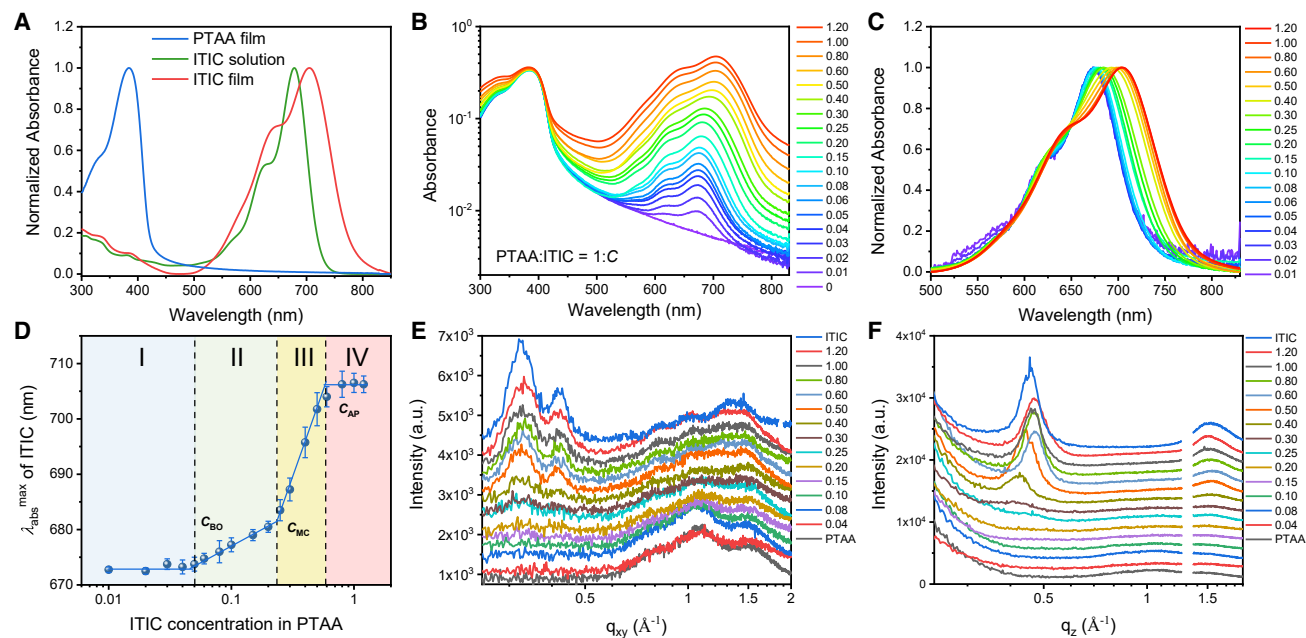


Figure 1. Study of PTAA:ITIC blend films by UV-vis absorption spectra based on the ASIMC method

(A) Normalized UV-vis absorption spectra of PTAA in film, ITIC in dilute solution, and ITIC in film.

(B) UV-vis spectra of PTAA:ITIC blend films with different concentrations of ITIC in PTAA.

(C) Normalized UV-vis spectra of ITIC after subtracting the PTAA background.

(D) Average ITIC main peak (0-0) location as a function of ITIC concentration in PTAA. Error bars represent standard deviation for four independent experiments.

(E and F) The corresponding 1D-GIWAXS intensity profiles of the PTAA:ITIC blend films along (E) in-plane and (F) out-of-plane directions.

sulfonic acid) sodium salt (PSS) modified substrates and at 1,000 rpm on zinc oxide (ZnO) modified substrates is shown in Figure S2. The films prepared by spin-coating at different speeds and different substrates showed four similar stages but with different turning concentrations, which indicates that the ASIMC method is also reproducible and sensitive.

To understand the different stages in Figure 1D, GIWAXS was performed on the blend films spin-coated at 1,000 rpm. The 2D-GIWAXS patterns of PTAA:ITIC with varying concentrations of ITIC in PTAA are presented in Figure S3. The corresponding line cuts along with the in-plane (q_{xy}) and out-of-plane (q_z) directions are shown in Figures 1E and 1F. The neat PTAA film exhibited a uniform ring at 1.1 \AA^{-1} and a π - π diffraction peak located around 1.5 \AA^{-1} .³⁹ Also, the scattering intensity was relatively weak for the PTAA neat film, suggesting that PTAA showed no preferred orientation with a low degree of order in the thin solid film. The neat ITIC film exhibited a π - π stacking around 1.53 \AA^{-1} in the out-of-plane direction and lamellar stacking around 0.42 \AA^{-1} in the in-plane direction, which suggests that ITIC molecules pack in a preferred “face-on” orientation. In addition, a diffraction peak at 0.33 \AA^{-1} in the in-plane direction was measured, which is ascribed to the formation of the backbone ordering structure of ITIC through π - π stacking between end caps.¹⁸ Since the diffraction of the π - π stacking for PTAA and ITIC overlaps, the backbone ordering and the lamellar stacking peaks are the critical signals for the determination of the packing structure of ITIC in the blend films.

At a very low ITIC concentration in PTAA (below 0.05), the $\lambda_{\text{abs}}^{\text{max}}$ of ITIC was measured to be around 673 nm, which is even lower than that of ITIC in chloroform solution

($\lambda_{\text{abs}}^{\text{max}} = 678 \text{ nm}$). Note that the maximum absorption wavelength of ITIC in dilute dichloromethane was 664 nm.¹ The lower $\lambda_{\text{abs}}^{\text{max}}$ for ITIC in the PTAA matrix compared with chloroform suggests that the PTAA surroundings showed less polar effect than the chloroform.⁴⁰ Meanwhile, no diffraction signals for ITIC were observed in GIWAXS at a low concentration of ITIC (Figures S3, 1E, and 1F). Therefore, we ascribed this part to a dissolved monomer stage, i.e., ITIC molecules are well mixed within the PTAA matrix, and little intermolecular interaction of ITIC molecules was found, which is consistent with the molecularly mixed features of the intermixed phase.^{12,28,32} We note that the limit of this molecular solution regime corresponds to the binodal if the film is under equilibrium conditions, analogous to the many bilayer interdiffusion experiments utilized previously.^{19,22,41,42}

When the ITIC concentration in PTAA was in the range of 0.05–0.20, the $\lambda_{\text{abs}}^{\text{max}}$ of the ITIC was found to be linearly correlated with the logarithmic ITIC concentration with an equation of $\lambda_{\text{abs}}^{\text{max}} = 688.2 + 11.1 \times \lg C$ ($R^2 = 0.998$) (Figure 1D), where C is the concentration of ITIC in PTAA and $\lambda_{\text{abs}}^{\text{max}}$ is the peak wavelength of ITIC at a concentration of C . Such a logarithmic relation of the absorption wavelength on concentration was also reported in micelles⁴³ and noble metal nanoparticle systems⁴⁴ and was ascribed to the formation of aggregates in the blend film. The measured increase in the $\lambda_{\text{abs}}^{\text{max}}$ of ITIC in the polymer blend indicates that ITIC molecules start aggregating. It was reported that ITIC molecules tend to form intermolecular networks through the end-cap π - π stack, with two main modes: chain-like and cluster-like aggregates.^{17,18} While in Figures 1E and 1F, when the ITIC concentration was over 0.15, weak backbone ordering and lamellar diffraction peaks at 0.33 and 0.42 \AA^{-1} in the in-plane direction appeared, and the intensities increased with the increase in ITIC concentration. In comparison to the UV-vis spectra, where shifting of the $\lambda_{\text{abs}}^{\text{max}}$ was seen when the ITIC concentration in PTAA was over 0.05, no backbone ordering peak was measured in GIWAXS for the films with ITIC concentrations below 0.15, which could be due to the low ITIC concentration and the signal being out of the detection limit. Nevertheless, the GIWAXS results confirmed the formation of the backbone ordering structure of ITIC in the PTAA:ITIC blend when the concentration was over 0.15 and the higher sensitivity of the UV-vis spectra method in measuring the formation of ITIC packing. Thus, we ascribed this logarithmic stage to forming backbone-ordered (chain-like) aggregates. The turning point ($C = 0.05$) that starts the linear increase in $\lambda_{\text{abs}}^{\text{max}}$ is then defined as the critical concentration for forming the backbone ordering structure (C_{BO}).

With further increase in the ITIC concentration to higher than 0.25, the second linearly increased $\lambda_{\text{abs}}^{\text{max}}$ versus logarithm ITIC concentration was measured with the equation $\lambda_{\text{abs}}^{\text{max}} = 720.2 + 61.8 \times \lg C$ ($R^2 = 0.995$). The more significant slope of this stage (stage III) results from the simultaneous presence of both new lamellar stacking and backbone ordering, supported by the GIWAXS results. In addition to the backbone and lamellar diffraction peaks at 0.33 and 0.42 \AA^{-1} in the in-plane direction, a new out-of-plane diffraction peak with higher intensity at around 0.42 \AA^{-1} was measured when the ITIC concentration exceeded 0.25, suggesting the formation of lamellar stacking of ITIC with an edge-on orientation at a higher concentration.¹⁸ Therefore, we ascribed this to the formation of molecular clusters (cluster-like aggregates), and the turning point ($C = 0.23$) was defined as the critical concentration for the formation of molecular clusters (C_{MC}).

With further increase in the ITIC concentration to over 0.60, the $\lambda_{\text{abs}}^{\text{max}}$ of ITIC in blend films is stabilized at about 706 nm, reaching the $\lambda_{\text{abs}}^{\text{max}}$ of the neat ITIC film (Figure 1A).

In Figure 1F, when the ITIC concentration exceeds 0.60, the lamellar packing diffraction peak shifts to 0.45 \AA^{-1} , corresponding to a smaller lamellar stacking distance, which can be ascribed to the formation of more condensed ITIC cluster domains. The more condensed ITIC aggregates are similar to the ITIC lamellar stacking in the neat film, in which ITIC would form an acceptor phase with 3D molecular packing.^{17,45} We, therefore, ascribed the final stage to forming the acceptor phase in the blend film. The ITIC concentration that starts forming the acceptor domain phase is then defined as the critical concentration for the acceptor phase ($C_{AP} = 0.59$). Over the C_{AP} , NFA molecules will cluster out from the polymer matrix and form NFA domains within the blend film. Thus, the C_{AP} is the maximum acceptor concentration in the intermixed phase. It should be noted that this value is an uncorrected composition in the intermixed phase since the polymer crystalline volume is unknown.

The thicknesses of the PTAA:ITIC blend films with different ITIC concentrations were also tested and the values are summarized in Table S2. The thickness as a function of ITIC concentration is plotted in Figure S4. When the ITIC concentration in PTAA was below 0.25 ± 0.9 to 33.9 ± 0.3 nm. Then, the thickness of the blend film increased with logarithmic ITIC concentration. Interestingly, the turning point in Figure S4 is similar to the C_{MC} in Figure 1D, suggesting different ITIC aggregation properties in the blend films.

NFA aggregation in polymer matrixes

Based on the above UV-vis and GIWAXS results measured for the PTAA:ITIC blend films, the aggregation structure and composition of ITIC in the PTAA matrix are illustrated in Figures 2A–2F. For the neat PTAA film, the pure polymer phase is surrounded by the amorphous polymer chains (Figure 2A).⁴⁶ PTAA is amorphous. However, the pure polymer phase was used here to represent devices that would use a polymer with a crystalline or paracrystalline phase.⁴⁷ When a small amount of ITIC is added, the ITIC molecules are entirely “dissolved” in the amorphous PTAA matrix. Only ITIC monomers are measured in this stage (Figure 2B, corresponding to stage I in Figure 1D). With the ITIC increase and the ITIC concentration higher than the C_{BO} , backbone ordering occurs through the end-cap π - π stacking between the ITIC molecules (Figure 2C, corresponding to stage II in Figure 1D). Then, in addition to the molecular ordering, an edge-on lamellar stacking of ITIC molecules occurs when the ITIC concentration is higher than C_{MC} in the blend films (Figure 2D, corresponding to stage III in Figure 1D). Finally, when the ITIC concentration exceeds the maximum acceptor composition in the intermixed phase, the acceptor phase forms within the blend film (Figure 2E, corresponding to stage IV in Figure 1D). Since the optimal donor:acceptor (D:A) weight ratio is needed to achieve the highest device performance, the nanomorphology within BHJ films typically shows three phases, comprising donor domain, acceptor domain, and intermixed phase (Figure 2F). Moreover, intermolecular interaction between ITIC molecules was evidenced to occur in the intermixed phase and the acceptor phase by the ASIMC method and concentration-dependent GIWAXS. With the increased ITIC concentration in the blend film, the number of ITIC molecules in the aggregation with molecular interaction increases in stages II and III and saturates when the acceptor phase forms.

Generality of the ASIMC method

To check the generality of this ASIMC method in determining the composition and aggregate structure of NFA molecules in PTAA, we then applied this method to other commonly used NFA molecules, including IT-M,⁴⁸ IT-4F,⁴⁹ IT-4Cl,⁵⁰ C8-IT-4F,⁵¹ and Y6.² Except for Y6, the other four compounds have a conjugated backbone identical to that of ITIC but slight differences in terminal substitution and alkyl side

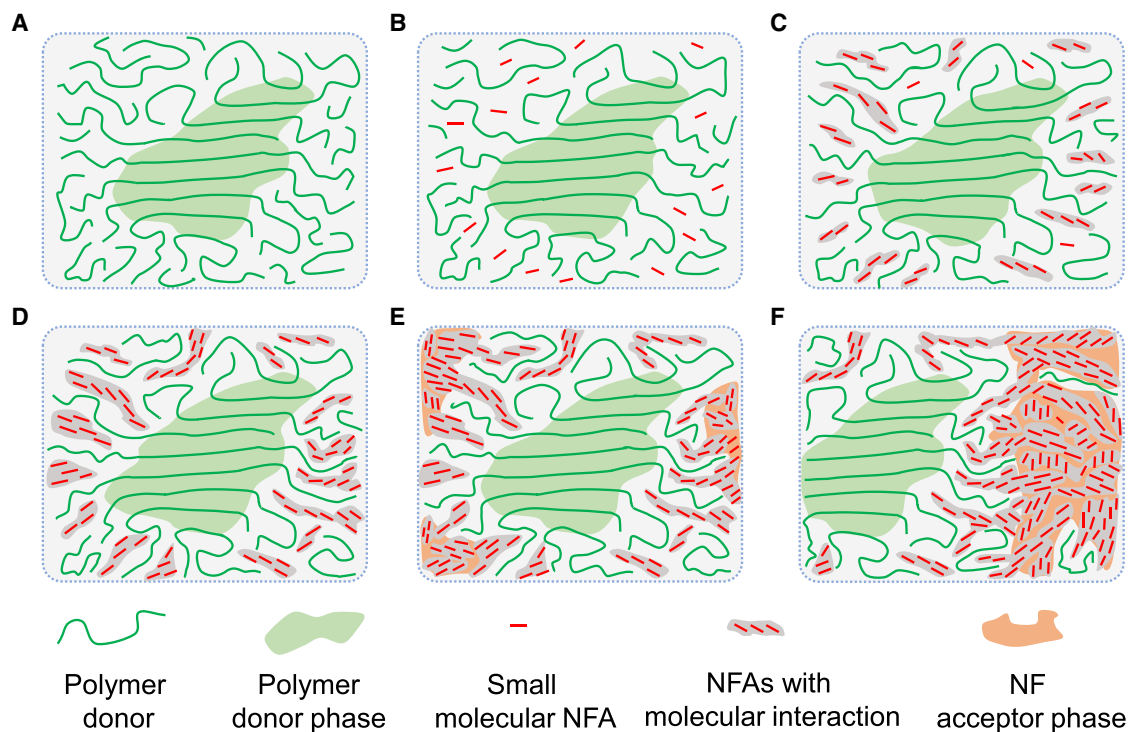


Figure 2. Schematic diagrams of the ASIMC method

(A) Neat polymer with the crystalline and amorphous region.
 (B) Monomer state of ITIC in the intermixed phase for stage I.
 (C) Backbone ordering state for stage II.
 (D) Molecular cluster state for stage III.
 (E) Acceptor phase arises in the blend film for stage IV.
 (F) The three-phase model with optimal D:A weight ratio.

chain. The chemical structures are also presented in [Figure S1](#). The detailed UV-vis absorption with different NFA content in the PTAA polymer matrix is shown in [Figures S5A and S5B](#) for IT-M and IT-4F and [Figures 3A–3C](#) for IT-4Cl, C8-IT-4F, and Y6, respectively. And the corresponding maximum absorption peak as a function of the logarithm of NFA concentration is shown in [Figures S5C and S5D](#) for IT-M and IT-4F and [Figures 3D–3F](#) for IT-4Cl, C8-IT-4F, and Y6, respectively.

The ITIC derivatives' blend films showed a $\lambda_{\text{abs}}^{\text{max}}$ similar to that in dilute chlorobenzene solution ([Figure S6A](#); 674, 691, 703, and 707 nm for IT-M, IT-4F, IT-4Cl, and C8-IT-4F, respectively) at a low concentration, which can be ascribed to the dissolved monomers in the polymer matrix. All the blend films showed the ASIMC phenomena. However, different transition processes were observed in these NFA blend films. Four different stages can be seen for the IT-M and IT-4F blend films ([Figure S5](#)), similar to ITIC shown in [Figure 1D](#). The critical concentrations were determined to be 0.12, 0.30, and 0.59 for IT-M and 0.08, 0.40, and 1.00 for IT-4F, respectively. The difference in critical concentration between ITIC, IT-M, and IT-4F can be understood by the different intermolecular interactions owing to their molecular structure differences.⁵²

Unlike the three NFAs mentioned above, as shown in [Figures 3A and 3D](#), the maximum peak of IT-4Cl turned out to be about 769 nm when the IT-4Cl

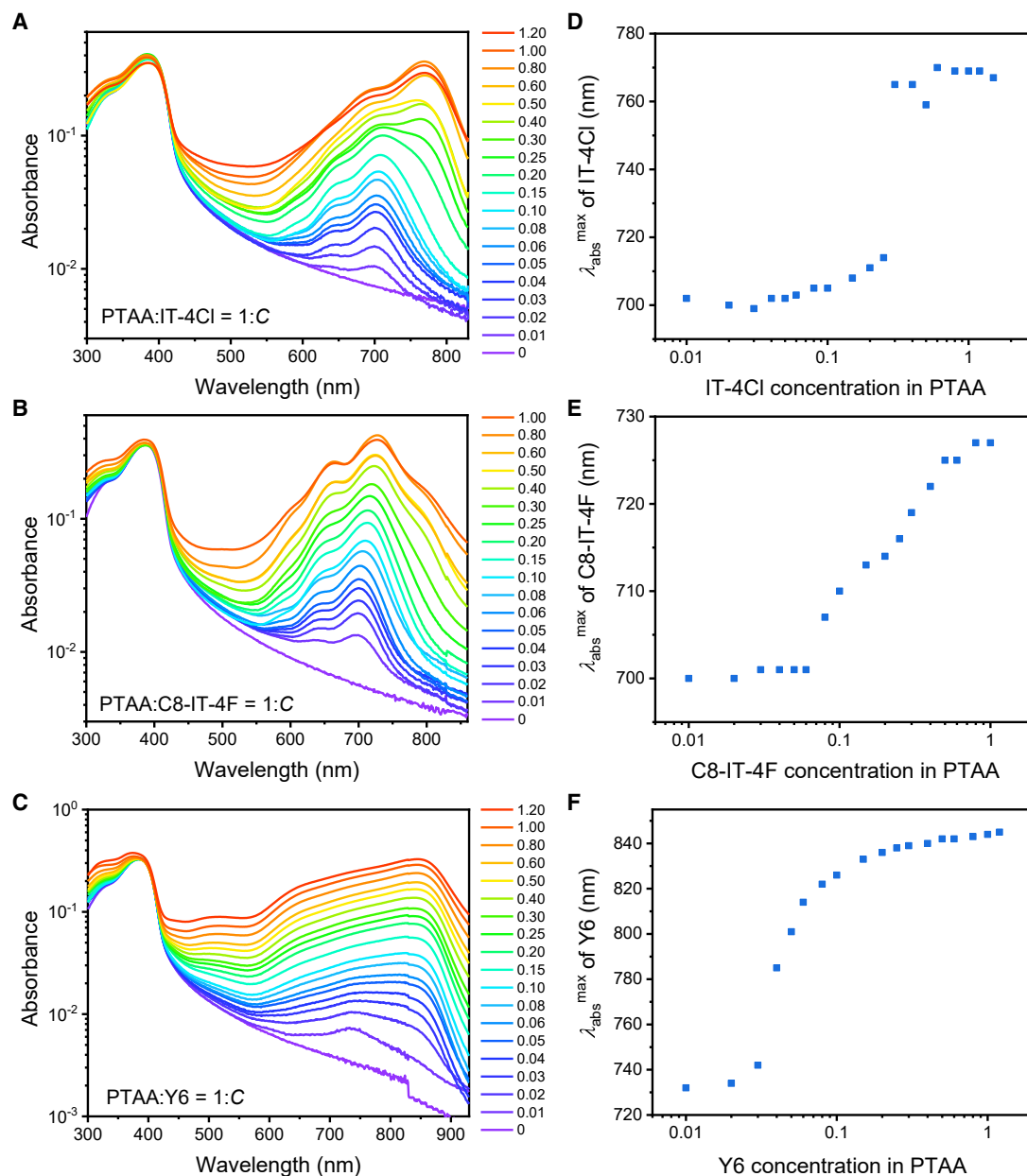


Figure 3. Generality of the ASIMC method

(A–C) UV-vis spectra of (A) PTAA:IT-4Cl, (B) PTAA:C8-IT-4F, and (C) PTAA:Y6 blend films with different NFA concentrations. (D–F) NFA main peak (0-0) location as a function of (D) IT-4Cl, (E) C8-IT-4F, and (F) Y6 concentration in PTAA.

concentration was higher than 0.30 for the PTAA:IT-4Cl blend films. Since the peak is similar to the neat IT-4Cl film (Figure S6B), we ascribed the low-energy band to acceptor phases due to the poor miscibility of IT-4Cl with PTAA (Table S3) and the higher crystallinity of IT-4Cl.⁵⁰ For PTAA:IT-4Cl blend films, only C_{BO} and C_{AP} were measured to be about 0.07 and 0.30. For PTAA:C8-IT-4F blend films, the $\lambda_{\text{abs}}^{\text{max}}$ as a function of the logarithm of C8-IT-4F (Figure 3E) showed a tendency similar to that of ITIC, IT-M, and IT-4F, but more aggregate states were measured in Figure 3B, and an additional shoulder peak around 780 nm was measured when the C8-IT-4F concentration in PTAA was higher than 0.40. This may be attributed to

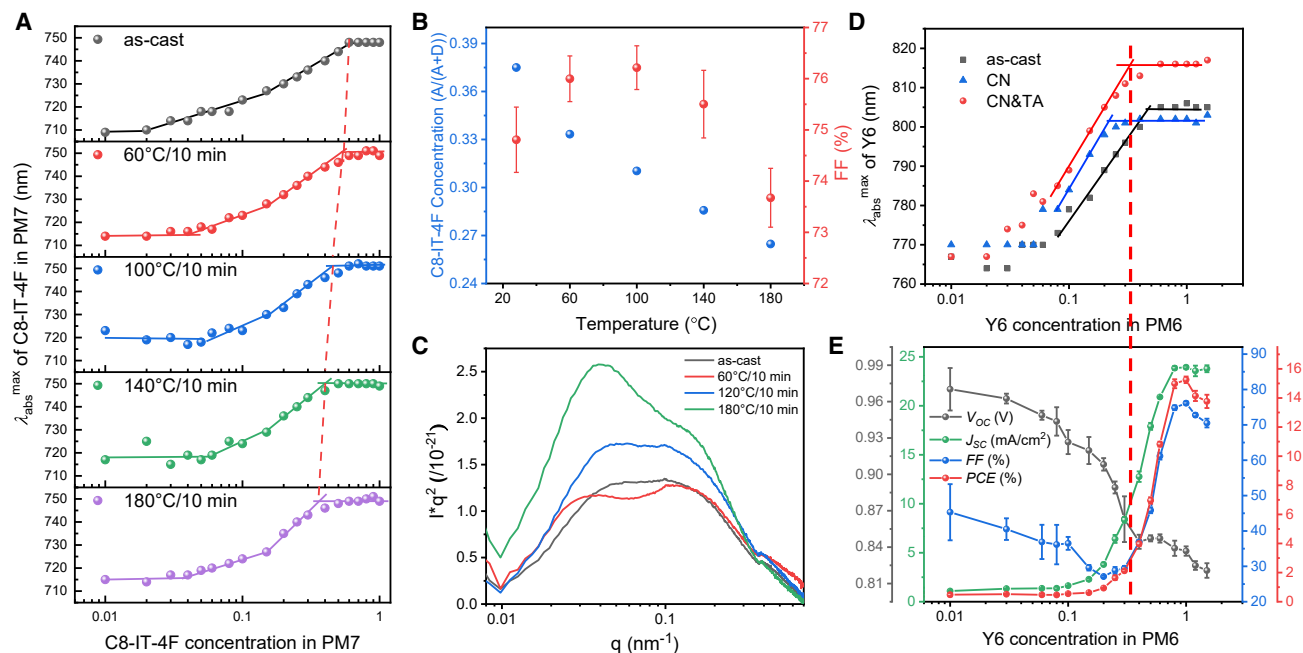


Figure 4. Study of PM7:C8-IT-4F and PM6:Y6 blend films by the ASIMC method

(A) C8-IT-4F main peak (0-0) location as a function of C8-IT-4F concentration for the as-cast blend films and the films with different thermal annealing temperatures. The variation of the C8-IT-4F concentration in the intermixed phase is indicated by the red dashed line.
 (B) Uncorrected C8-IT-4F concentration in the intermixed phase ($A/(D + A)$) obtained by the ASIMC method at different temperatures, and average FF of the PM7:C8-IT-4F devices at different temperatures. The average values of FF were calculated from more than eight independent cells. Error bars represent standard deviation.
 (C) R-SoXS scattering profiles of PM7:C8-IT-4F (D:A = 1:1) with the different thermal conditions at 285.2 eV.
 (D) Y6 main peak (0-0) location as a function of Y6 concentration for as-cast, with 0.5% CN (CN)- and 0.5% CN and 100°C/10 min (CN&TA)-treated films.
 (E) The average photovoltaic parameters (over two independent cells), V_{OC} , J_{SC} , FF, and PCE values, as a function of Y6 concentration. The red dashed line in (D) and (E) is used to indicate the relationship between the Y6 concentration in the intermixed phase and the photovoltaic performance of PM6:Y6 blend films with different Y6 concentrations.

the lower steric hindrance of the alkyl side chain and the different distances of different types of π - π stacking.^{51,53} In PTAA:Y6 films (Figures 3C and 3F), when the Y6 concentration is 0.01, the maximum absorption of Y6 is 732 nm, which is similar to that in solution (731 nm). However, a shoulder absorption peak at about 830 nm was observed even at a low concentration, suggesting Y6 aggregates in thin solid films. This may be due to the poor miscibility of Y6 with PTAA (Table S3) and the higher crystallinity of Y6.⁵⁴ These results demonstrate that molecular structure has a significant influence on the aggregation behaviors of NFA molecules.

Structure-photovoltaic performance relationship

Next, we applied the ASIMC method to study the practical photovoltaic blend films. The PM7:C8-IT-4F and PM6:Y6 systems were selected (chemical structures are presented in Figure S1). The fabricated PM7:C8-IT-4F and PM6:Y6 devices at the optimized conditions exhibited PCEs of about 14% and 16% (Table S4), respectively, which are in good accordance with the PCEs reported in the literature.^{2,51} The blend films with different NFAs were spin-coated and post-processed with the same recipe for the optimized device.

The λ_{abs}^{max} of C8-IT-4F as a function of C8-IT-4F concentration in the as-cast PM7:C8-IT-4F blend films is plotted in Figure 4A. Four stages can also be distinguished in this figure. At a low concentration of 0.01, the peak of C8-IT-4F was measured to be

709 nm, which is close to that of the C8-IT-4F monomer state's peak in dilute solution (707 nm, Figure S6). Then, the peak red shifts slowly to 727 nm when the concentration of C8-IT-4F in PM7 reaches about 0.15, which suggests that, in PM7:C8-IT-4F blend films, intermolecular interactions already form even at very low concentration of C8-IT-4F. Between 0.20 and 0.60, a higher slope was observed. When the C8-IT-4F concentration reached about 0.60 in PM7, the peak no longer changed. Thus, the uncorrected concentration of C8-IT-4F in the intermixed phase of the as-cast PM7:C8-IT-4F blend films is 37.5%.

As discussed above, the acceptor concentration in the intermixed phase is significant for photovoltaic performance in OPVs, and the post-treatment would influence this concentration. Therefore, we also examined the concentration-dependent UV-vis absorption of the series of blend films at different thermal annealing temperatures. As shown in Figure 4A, the main peaks of C8-IT-4F change with thermal annealing temperature. The C8-IT-4F concentration in the intermixed phase decreases as the temperature increases (red dashed line in Figure 4A, the corresponding data are presented in Figure 4B), indicating that the intermixed phase domain purities increase with the thermal annealing temperature. Combined with the photovoltaic performance of the conventional device (indium-tin oxide (ITO)/poly(3,4-ethylene-dioxythiophene):poly(styrene sulfonate) (PEDOT:PSS)/PM7:C8-IT-4F/PFN-Br/Al) at different thermal annealing temperatures (data are summarized in Table S4; fill factor [FF] values are plotted in Figure 4B), the correct C8-IT-4F concentration in the intermixed phase is highly needed to get a higher FF. Phases that are too impure or too pure would result in lower FF.^{13,19}

R-SoXS was used to investigate the domain purity.^{28,55} A relative comparison of composition variation and thus indirectly the domain purity could be obtained by integrating the scattering profiles (the total scattering intensity). Figure 4C shows the R-SoXS data of PM7:C8-IT-4F (D:A = 1:1) blend films with different thermal annealing conditions at the carbon K-edge (~285 eV). The scattering intensities increase with the thermal annealing temperature, suggesting that the domain purities increase with thermal annealing temperature.²¹ The overall root-mean-square composition variations are estimated to be 0.88, 0.92, 0.97, and 1 for the as-cast, 60°C, 120°C, and 180°C 10-min thermal-annealing (TA) PM7:C8-IT-4F (D:A = 1:1) blend films, respectively. The R-SoXS result shows the same tendency as the C8-IT-4F concentration in the intermixed phase obtained by the ASIMC method.

PM6:Y6 blend films need solvent additive and thermal annealing to optimize the morphology for better photovoltaic performance.² Figure 4D shows Y6's main peak in PM6:Y6 blend films as a function of Y6 concentration under different processing conditions. However, at low Y6 concentration in the PM6:Y6 blend films, the main peak of Y6 is around 770 nm, which is red shifted compared with 731 nm of the Y6 monomer in dilute chloroform solution. This may relate to the unique packing of Y6 molecules.^{54,56} More work needs to be conducted on this in the future, as it is not within the scope of this work. Herein, we focused on only the concentration of Y6 in the intermixed phase, which changes with the optimized processes. As shown in Figure 4D, the uncorrected Y6 concentration in the intermixed phase was about 0.33, 0.19, and 0.25 for the as-cast film (as-cast), the film with 0.5% 1-chloronaphthalene (CN), and the film with 0.5% CN and 100°C/10 min (CN&TA), respectively. According to the photovoltaic performance of the conventional devices (Table S4) and the Y6 concentration in the intermixed phase with different treatments, the domain purities in as-cast and CN-treated blend films are too impure and too pure, respectively.¹³ The CN&TA-treated device

possessed the proper Y6 concentration in the intermixed phase, which is in the range of the percolation threshold, to get higher FF and better PCE.¹⁹

R-SoXS was also used to study PM6:Y6 blend films under the different processing conditions. R-SoXS scattering profiles of PM6:Y6 systems are shown in Figure S7. When accounting for fluorescence background and the low scattering contrast, we find that the as-cast PM6:Y6 films have the lowest and the CN-treated films the highest intensity. The R-SoXS results of PM6:Y6 blend films also show the same tendency as the results obtained by the ASIMC method (Figure 4D).

GIWAXS was used to study the PM6:Y6 blend films treated with CN&TA. 2D-GIWAXS patterns are shown in Figure S8. Like the previous report, the π - π stacking distance of PM6 and Y6 is about 3.67 and 3.61 Å, respectively.² Therefore, π - π stacking distance of the combined PM6/Y6 signal was extracted and plotted in Figure S9 as a function of Y6 concentration. The π - π stacking distance was around 3.67 Å when the Y6 fraction was below 0.20, and the distance was around 3.61 Å when the Y6 fraction exceeded 0.30, suggesting that the Y6 domain phase arises after the Y6 concentration exceeds 0.30. The GIWAXS result is also consistent with the result obtained by the ASIMC method.

The photovoltaic performance of PM6:Y6 blend films with different Y6 concentrations was also tested by using an inverted device structure (ITO/ZnO/active layer/MoO_x/Ag). The tendency of the photovoltaic parameters, V_{OC} , J_{SC} , FF, and PCE, is plotted as a function of Y6 concentration in Figure 4E. The V_{OC} are around 0.95 V (show a slight decrease tendency) when the Y6 concentration is below 0.10, then decrease quickly between 0.10 and 0.30, and show a slight tendency to decrease around 0.84 V when the concentration of Y6 exceeds 0.30. We found that the V_{OC} approach constant values when the acceptor domain phase arises in the blend films according to the ASIMC method. The J_{SC} increase slightly around 1.3 mA/cm² when Y6 concentration is below 0.10, then increase gradually between 0.10 and 0.60, and finally approach saturation. The increased absorption intensity of Y6 in the films is one reason for the increased J_{SC} . And external quantum efficiency (EQE) curves of PM6:Y6 devices with different Y6 concentrations are also added in Figure S10A. The calculated current densities (J_{cal}), which are integrated from EQE curves and the AM 1.5 G solar spectrum, as a function of Y6 concentration (Figure S10B) also present a similar tendency compared with J_{SC} versus C_{Y6} . As presented in Figure S10A, the EQE values of PM6 increase with the Y6 concentration, which suggests that more efficient exciton dissociation and charge transport are the other effects contributing to the increased J_{SC} . Around the Y6 concentration in the intermixed phase, the ratio of change of J_{SC} is the largest. The FF decreases when the Y6 concentration is below 0.20, suggesting that the isolated Y6 aggregates may function as traps in the blend films. And then, The FF gradually increases after 0.30 and reaches the highest value at 1.00 concentration of Y6. The resulting PCEs are below 1% when Y6 concentration is 0.20, then increase gradually from 0.20 to 0.80, and are over 15% when Y6 concentration is 1. The onset of FFs and PCEs is consistent with the Y6 concentration in the intermixed phase. Therefore, the ASIMC results show a good relationship with the devices' photovoltaic performance.

DISCUSSION

In summary, this study demonstrates an experimental approach to revealing NFA concentration-dependent molecular aggregation in OPV blend films. The methodology is based on commonly used UV-vis absorption spectroscopy to study the

molecular states of NFAs in blend films as a function of NFA concentration. In the model blend film, PTAA:ITIC, the NFAs show different molecular aggregated states in the polymer matrix with different NFA contents: monomer, molecular backbone, molecular cluster, and acceptor phase. In particular, intermolecular interactions were proved to occur between the NFA molecules in the intermixed phase of BHJ films. And the NFA concentration in the intermixed phase was also determined. In real photovoltaic devices, PM7:C8-IT-4F and PM6:Y6, the ASIMC method was used to study the effects of process and post-treatment conditions on the composition in the intermixed phase and to relate structure and performance.

In a broader context, we believe that the methodology is widely applicable to studying properties of disordered intermixed heterointerfaces of organic electronic devices that consist of two materials with different spectral absorptions. With the information on concentration-dependent molecular aggregated states in blend films, more clarity on the photophysics and charge transport processes would be obtained by combining other characterization techniques. In addition, we believe that the evolution of concentration-dependent molecular packing and aggregation during aging could be explored to understand the relationship with the burn-in loss of OPVs. In the future, the ASIMC method is expected to help workers understand the molecular interactions between NFAs and help disclose the structure-property relationship of BHJ OPVs under non-equilibrium conditions.

EXPERIMENTAL PROCEDURES

Resource availability

Lead contact

Further information and requests for resources and materials should be directed to and will be fulfilled by the lead contact, Chang-Qi Ma (cqma2011@sinano.ac.cn).

Materials availability

This study did not generate new unique materials.

Data and code availability

All of the data supporting the results are presented in the main text and [supplemental information](#). Further information and requests for additional data should be directed to the [lead contact](#).

Materials

PTAA (15K–50K) was purchased from Xi'an Polymer Light Technology Corp. ITIC, IT-M, IT-4F, IT-4Cl, Y6, PM7, PM6, and PFN-Br were purchased from Solarmer Materials (Beijing). C8-IT-4F was purchased from Hyper, Inc. (China).

Blend films with different NFA concentration

Glass substrates were sequentially cleaned with deionized water, acetone, and isopropanol by sonication. After being dried with compressed N₂ gas, the glass substrate was treated with UV-ozone for 30 min. PSS (1 mg/mL, in water) layers were spin-coated at 3,000 rpm and dried at 130°C for 10 min. Then, the substrates were transferred into a glove box with N₂. Blend films with different polymer:NFA weight ratios ([Table S1](#)) were spin-coated on the substrates. The concentration of PTAA was 10 mg/mL in CB solution. The PTAA:NFA solution was spin-coated at 2,000 or 1,000 rpm. The concentration of PM7 in PM7:C8-IT-4F CB solution was 12 mg/mL. The PM7:C8-IT-4F solution was spin-coated at 2,000 rpm. The PM7:C8-IT-4F blend films were then annealed at an elevated temperature for 10 min. The concentration of PM6 in the PM6:Y6 chloroform solution was 8.2 mg/

mL. And 0.5% CN (volume fraction) process additives and thermal annealing (100°C for 10 min) were used to optimize the morphology. The PM6:Y6 solution was spin-coated at 3,000 rpm.

Photovoltaic device fabrication

The NFA-based devices were fabricated with a conventional structure (ITO/PEDOT:PSS/active layer/PFN-Br/Al). A 30-nm-thick PEDOT:PSS (Bayer Baytron 4083) anode buffer layer was spin-coated onto the ITO substrates and dried by baking in an oven at 150°C for 10 min. The active layer was then deposited on top of the PEDOT:PSS by spin-coating for 40 s in a nitrogen-filled glove box at about 28°C. For PM7:C8-IT-4F devices, the optimal donor/acceptor ratio was 1:1. For PM6:Y6 devices, the optimal donor/acceptor ratio was 1:1.2. PFN-Br (0.5 mg/mL in methane) was deposited on top of the active layer as a cathode buffer layer. An Al (100 nm) top electrode was evaporated under vacuum at a pressure of ca. 4×10^{-4} Pa. The effective area of one cell was 4 mm².

The devices of PM6:Y6 blend films with different Y6 concentrations were fabricated with an inverted device structure (ITO/ZnO/active layer/MoO_x/Ag). A ZnO cathode layer of approximately 30 nm was prepared by spin-coating (at 3,000 rpm) a precursor solution prepared from 0.45 M zinc acetate dehydrate in 0.45 M ethanolamine and 2-methoxy ethanol. After the electrical contact was cleaned, ZnO-coated ITO glass substrates were immediately baked in the air at 200°C for 1 h. Subsequently, the PM6:Y6 blend solutions with different Y6 concentrations were spin-coated at 3,000 rpm for 60 s on top of the ZnO layer. A MoO_x (10 nm) anode layer and Ag (160 nm) top electrode were evaporated thermally.

Instruments and measurement

UV-vis absorption spectra of BHJ films were measured with a PerkinElmer Lambda 750 at room temperature. The current density-voltage (*J*-*V*) characteristics of the non-fullerene OPVs were recorded in a glove box filled with N₂ with a Keithley 2400 source meter under illumination with simulated AM 1.5 G sunlight using an SS-F5-3A (Enli Technology) solar simulator (AAA grade, 50 × 50 mm photo-beam size). A 2 × 2 cm² monocrystalline silicon reference cell (SRC-00019, covered with a KG5 filter window) was purchased from Enli Technology Co., Ltd. GIWAXS measurements were performed in a Xeuss 3.0 SAXS/WAXS system with a wavelength of $\lambda = 1.341$ Å at a Vacuum Interconnected Nanotech Workstation (Nano-X). R-SoXS measurements were performed at a beamline 11.0.1.2 (Advanced Light Source, Lawrence Berkeley National Laboratory, Berkeley, CA).

SUPPLEMENTAL INFORMATION

Supplemental information can be found online at <https://doi.org/10.1016/j.xcrp.2022.100983>.

ACKNOWLEDGMENTS

This work was supported by the National Natural Science Foundation of China (NSFC) (22109172, 22075315, 22135001). The authors are grateful for the technical support for Nano-X from Suzhou Institute of Nano-Tech and Nano-Bionics, Chinese Academy of Sciences (A2107). This work was also supported by Jiangsu Key Laboratory of Advanced Functional Polymer Design and Application, Soochow University (KJS2117). R-SoXS data were acquired at beamlines 11.0.1.2 at the Advanced Light Source, LBNL, supported by the Director, Office of Science, Office of Basic Energy Sciences, of the US Department of Energy under contract

DE-AC02-05CH11231. Work at NCSU is supported by ONR grant N0001420 12155.

AUTHOR CONTRIBUTIONS

J.F. and C.-Q.M. conceived the idea and designed the experiment. J.F. acquired the UV-vis data and J-V data. Z.W. and H.A. performed R-SoXS measurements and evaluated the data. Y.Y.C. and Q.Z. performed GIWAXS measurements. J.Q.Z., L.Y.Z., and Z.X.W. helped to analyze the GIWAXS results and concentration-dependent UV-vis. J.F. and C.-Q.M. prepared the manuscript. Z.W., H.A., and Z.X.W. revised the manuscript. M.J.Z. and Z.C. were involved in discussions and helped revise the manuscript. All the authors discussed the results and commented on the manuscript.

DECLARATION OF INTERESTS

The authors declare no competing interests.

Received: March 29, 2022

Revised: June 6, 2022

Accepted: June 17, 2022

Published: July 12, 2022

REFERENCES

- Lin, Y., Wang, J., Zhang, Z.G., Bai, H., Li, Y., Zhu, D., and Zhan, X. (2015). An electron acceptor challenging fullerenes for efficient polymer solar cells. *Adv. Mater.* 27, 1170–1174. <https://doi.org/10.1002/adma.201404317>.
- Yuan, J., Zhang, Y., Zhou, L., Zhang, G., Yip, H.L., Lau, T.K., Lu, X., Zhu, C., Peng, H., Johnson, P.A., et al. (2019). Single-junction organic solar cell with over 15% efficiency using fused-ring acceptor with electron-deficient core. *Joule* 3, 1140–1151. <https://doi.org/10.1016/j.joule.2019.01.004>.
- Zheng, Z., Yao, H., Ye, L., Xu, Y., Zhang, S., and Hou, J. (2020). PBDB-T and its derivatives: a family of polymer donors enables over 17% efficiency in organic photovoltaics. *Mater. Today* 35, 115–130. <https://doi.org/10.1016/j.mattod.2019.10.023>.
- Cui, Y., Xu, Y., Yao, H., Bi, P., Hong, L., Zhang, J., Zu, Y., Zhang, T., Qin, J., Ren, J., et al. (2021). Single-junction organic photovoltaic cell with 19% efficiency. *Adv. Mater.* 33, 2102420. <https://doi.org/10.1002/adma.202102420>.
- Zhang, M., Zhu, L., Zhou, G., Hao, T., Qiu, C., Zhao, Z., Hu, Q., Larson, B.W., Zhu, H., Ma, Z., et al. (2021). Single-layered organic photovoltaics with double cascading charge transport pathways: 18% efficiencies. *Nat. Commun.* 12, 309. <https://doi.org/10.1038/s41467-020-20580-8>.
- Li, C., Zhou, J., Song, J., Xu, J., Zhang, H., Zhang, X., Guo, J., Zhu, L., Wei, D., Han, G., et al. (2021). Non-fullerene acceptors with branched side chains and improved molecular packing to exceed 18% efficiency in organic solar cells. *Nat. Energy* 6, 605–613. <https://doi.org/10.1038/s41560-021-00820-x>.
- Wang, Z., Gao, K., Kan, Y., Zhang, M., Qiu, C., Zhu, L., Zhao, Z., Peng, X., Feng, W., Qian, Z., et al. (2021). The coupling and competition of crystallization and phase separation, correlating thermodynamics and kinetics in OPV morphology and performances. *Nat. Commun.* 12, 332. <https://doi.org/10.1038/s41467-020-20515-3>.
- Lee, H., Park, C., Sin, D.H., Park, J.H., and Cho, K. (2018). Recent advances in morphology optimization for organic photovoltaics. *Adv. Mater.* 30, 1800453. <https://doi.org/10.1002/adma.201800453>.
- Gao, K., Deng, W., Xiao, L., Hu, Q., Kan, Y., Chen, X., Wang, C., Huang, F., Peng, J., Wu, H., et al. (2016). New insight of molecular interaction, crystallization and phase separation in higher performance small molecular solar cells via solvent vapor annealing. *Nano Energy* 30, 639–648. <https://doi.org/10.1016/j.nanoen.2016.10.031>.
- Richter, L.J., Delongchamp, D.M., and Amassian, A. (2017). Morphology development in solution-processed functional organic blend films: an in situ viewpoint. *Chem. Rev.* 117, 6332–6366. <https://doi.org/10.1021/acs.chemrev.6b00618>.
- Liang, R.Z., Babics, M., Seitkhan, A., Wang, K., Geraghty, P.B., Lopatin, S., Cruciani, F., Firdaus, Y., Caporuscio, M., Jones, D.J., and Beaujuge, P.M. (2018). Additive-morphology interplay and loss channels in “all-small-molecule” bulk-heterojunction (BHJ) solar cells with the nonfullerene acceptor IDTTBM. *Adv. Funct. Mater.* 28, 1705464. <https://doi.org/10.1002/adfm.201705464>.
- Burke, T.M., and McGehee, M.D. (2014). How high local charge carrier mobility and an energy cascade in a three-phase bulk heterojunction enable >90% quantum efficiency. *Adv. Mater.* 26, 1923–1928. <https://doi.org/10.1002/adma.201304241>.
- Ye, L., Collins, B.A., Jiao, X., Zhao, J., Yan, H., and Ade, H. (2018). Miscibility–function relations in organic solar cells: significance of optimal miscibility in relation to percolation. *Adv. Energy Mater.* 8, 1703058. <https://doi.org/10.1002/aenm.201703058>.
- Collins, B.A., Gann, E., Guignard, L., He, X., McNeill, C.R., and Ade, H. (2010). Molecular miscibility of polymer-fullerene blends. *J. Phys. Chem. Lett.* 1, 3160–3166. <https://doi.org/10.1021/jz101276h>.
- Limbu, S., Pont, S., Doust, A.B., Kwon, S., Fuller, P., Tan, E., Durrant, J.R., and Kim, J.S. (2019). Impact of initial bulk-heterojunction morphology on operational stability of polymer:fullerene photovoltaic cells. *Adv. Mater. Inter.* 6, 1801763. <https://doi.org/10.1002/admi.201801763>.
- Ferron, T., Waldrip, M., Pope, M., and Collins, B.A. (2019). Increased charge transfer state separation: via reduced mixed phase interface in polymer solar cells. *J. Mater. Chem. A* 7, 4536–4548. <https://doi.org/10.1039/c8ta12336e>.
- Han, G., Guo, Y., Song, X., Wang, Y., and Yi, Y. (2017). Terminal π - π Stacking determines three-dimensional molecular packing and isotropic charge transport in an A- π -A electron acceptor for non-fullerene organic solar cells. *J. Mater. Chem. C* 5, 4852–4857. <https://doi.org/10.1039/c7tc01310h>.
- Mai, J., Xiao, Y., Zhou, G., Wang, J., Zhu, J., Zhao, N., Zhan, X., and Lu, X. (2018). Hidden structure ordering along backbone of fused-ring electron acceptors enhanced by ternary bulk heterojunction. *Adv. Mater.*

- 30, 1802888. <https://doi.org/10.1002/adma.201802888>.
19. Ghasemi, M., Balar, N., Peng, Z., Hu, H., Qin, Y., Kim, T., Rech, J.J., Bidwell, M., Mask, W., McCulloch, I., et al. (2021). A molecular interaction-diffusion framework for predicting organic solar cell stability. *Nat. Mater.* 20, 525–532. <https://doi.org/10.1038/s41563-020-00872-6>.
 20. Gao, M., Liang, Z., Geng, Y., and Ye, L. (2020). Significance of thermodynamic interaction parameters in guiding the optimization of polymer:nonfullerene solar cells. *Chem. Commun.* 56, 12463–12478. <https://doi.org/10.1039/d0cc04869k>.
 21. Ye, L., Li, S., Liu, X., Zhang, S., Ghasemi, M., Xiong, Y., Hou, J., and Ade, H. (2019). Quenching to the percolation threshold in organic solar cells. *Joule* 3, 443–458. <https://doi.org/10.1016/j.joule.2018.11.006>.
 22. Ghasemi, M., Hu, H., Peng, Z., Rech, J.J., Angunawela, I., Carpenter, J.H., Stuard, S.J., Wadsworth, A., McCulloch, I., You, W., and Ade, H. (2019). Delineation of thermodynamic and kinetic factors that control stability in non-fullerene organic solar cells. *Joule* 3, 1328–1348. <https://doi.org/10.1016/j.joule.2019.03.020>.
 23. Du, X., Heumueller, T., Gruber, W., Almora, O., Classen, A., Qu, J., He, F., Unruh, T., Li, N., and Brabec, C.J. (2020). Unraveling the microstructure-related device stability for polymer solar cells based on nonfullerene small-molecular acceptors. *Adv. Mater.* 32, 1908305. <https://doi.org/10.1002/adma.201908305>.
 24. Li, N., Perea, J.D., Kassar, T., Richter, M., Heumueller, T., Matt, G.J., Hou, Y., Güldal, N.S., Chen, H., Chen, S., et al. (2017). Abnormal strong burn-in degradation of highly efficient polymer solar cells caused by spinodal donor-acceptor demixing. *Nat. Commun.* 8, 14541. <https://doi.org/10.1038/ncomms14541>.
 25. Shih, M.C., Huang, B.C., Lin, C.C., Li, S.S., Chen, H.A., Chiu, Y.P., and Chen, C.W. (2013). Atomic-scale interfacial band mapping across vertically phased-separated polymer/fullerene hybrid solar cells. *Nano Lett.* 13, 2387–2392. <https://doi.org/10.1021/nl400091f>.
 26. Ferron, T., Pope, M., and Collins, B.A. (2017). Spectral analysis for resonant soft X-ray scattering enables measurement of interfacial width in 3D organic nanostructures. *Phys. Rev. Lett.* 119, 167801. <https://doi.org/10.1103/physrevlett.119.167801>.
 27. Treat, N.D., Varotto, A., Takacs, C.J., Batara, N., Al-Hashimi, M., Heeney, M.J., Heeger, A.J., Wudl, F., Hawker, C.J., and Chabincyn, M.L. (2012). Polymer-fullerene miscibility: a metric for screening new materials for high-performance organic solar cells. *J. Am. Chem. Soc.* 134, 15869–15879. <https://doi.org/10.1021/ja305875u>.
 28. Collins, B.A., Li, Z., Tumbleston, J.R., Gann, E., McNeill, C.R., and Ade, H. (2013). Absolute measurement of domain composition and nanoscale size distribution explains performance in PTB7:PC71bm solar cells. *Adv. Energy Mater.* 3, 65–74. <https://doi.org/10.1002/aenm.201200377>.
 29. Peng, Z., Jiao, X., Ye, L., Li, S., Rech, J.J., You, W., Hou, J., and Ade, H. (2018). Measuring temperature-dependent miscibility for polymer solar cell blends: an easily accessible optical method reveals complex behavior. *Chem. Mater.* 30, 3943–3951. <https://doi.org/10.1021/acs.chemmater.8b00889>.
 30. Bartel, J.A., Beiley, Z.M., Hoke, E.T., Mateker, W.R., Douglas, J.D., Collins, B.A., Tumbleston, J.R., Graham, K.R., Amassian, A., Ade, H., et al. (2013). The importance of fullerene percolation in the mixed regions of polymer-fullerene bulk heterojunction solar cells. *Adv. Energy Mater.* 3, 364–374. <https://doi.org/10.1002/aenm.201200637>.
 31. Yin, W., and Dadmun, M. (2011). A new model for the morphology of p3ht/pcbm organic photovoltaics from small-angle neutron scattering: rivers and streams. *ACS Nano* 5, 4756–4768. <https://doi.org/10.1021/nn200744q>.
 32. Ruderer, M.A., Meier, R., Porcar, L., Cubitt, R., and Müller-Buschbaum, P. (2012). Phase separation and molecular intermixing in polymer-fullerene bulk heterojunction thin films. *J. Phys. Chem. Lett.* 3, 683–688. <https://doi.org/10.1021/jz300039h>.
 33. Tumbleston, J.R., Yang, L., You, W., and Ade, H. (2014). Morphology linked to miscibility in highly amorphous semi-conducting polymer/fullerene blends. *Polymer* 55, 4884–4889. <https://doi.org/10.1016/j.polymer.2014.07.051>.
 34. Cheng, P., Wang, H.C., Zhu, Y., Zheng, R., Li, T., Chen, C.H., Huang, T., Zhao, Y., Wang, R., Meng, D., et al. (2020). Transparent hole-transporting frameworks: a unique strategy to Design high-performance semitransparent organic photovoltaics. *Adv. Mater.* 32, 2003891. <https://doi.org/10.1002/adma.202003891>.
 35. Chen, Z., Lohr, A., Saha-Möller, C.R., and Würthner, F. (2009). Self-assembled π -stacks of functional dyes in solution: structural and thermodynamic features. *Chem. Soc. Rev.* 38, 564–584. <https://doi.org/10.1039/b809359h>.
 36. Spano, F.C., and Silva, C. (2014). H- and J-aggregate behavior in polymeric semiconductors. *Annu. Rev. Phys. Chem.* 65, 477–500. <https://doi.org/10.1146/annurev-physchem-040513-103639>.
 37. Würthner, F., Kaiser, T.E., and Saha-Möller, C.R. (2011). J-aggregates: from serendipitous discovery to supramolecular engineering of functional dye materials. *Angew. Chem. Int. Ed. Engl.* 50, 3376–3410. <https://doi.org/10.1002/anie.201002307>.
 38. Ma, C.Q., Mena-Osteritz, E., Wunderlin, M., Schulz, G., and Bäuerle, P. (2012). 2, 2':3', 2''-Terthiophene-based all-thiophene dendrons and dendrimers: synthesis, structural characterization, and properties. *Chemistry* 18, 12880–12901. <https://doi.org/10.1002/chem.201200231>.
 39. Xu, G., Xue, R., Stuard, S.J., Ade, H., Zhang, C., Yao, J., Li, Y., and Li, Y. (2021). Reducing energy disorder of hole transport layer by charge transfer complex for high performance p-i-n perovskite solar cells. *Adv. Mater.* 33, 2006753. <https://doi.org/10.1002/adma.202006753>.
 40. Reichardt, C. (2004). Solvent effects on the absorption spectra of organic compounds. In *Solvents and Solvent Effects in Organic Chemistry* (Wiley-VCH Verlag GmbH & Co. KGaA), pp. 329–388.
 41. Ye, L., Hu, H., Ghasemi, M., Wang, T., Collins, B.A., Kim, J.H., Jiang, K., Carpenter, J.H., Li, H., Li, Z., et al. (2018). Quantitative relations between interaction parameter, miscibility and function in organic solar cells. *Nat. Mater.* 17, 253–260. <https://doi.org/10.1038/s41563-017-0005-1>.
 42. Zhu, Y., Gadisa, A., Peng, Z., Ghasemi, M., Ye, L., Xu, Z., Zhao, S., and Ade, H. (2019). Rational strategy to stabilize an unstable high-efficiency binary nonfullerene organic solar cells with a third component. *Adv. Energy Mater.* 9, 1900376. <https://doi.org/10.1002/aenm.201900376>.
 43. Carey, M.C., and Small, D.M. (1969). Micellar properties of dihydroxy and trihydroxy bile salts: effects of counterion and temperature. *J. Colloid Interface Sci.* 31, 382–396. [https://doi.org/10.1016/0021-9797\(69\)90181-7](https://doi.org/10.1016/0021-9797(69)90181-7).
 44. Zhu, J., Zhao, B.Z., Qi, Y., Li, J.J., Li, X., and Zhao, J.W. (2018). Colorimetric determination of Hg(II) by combining the etching and aggregation effect of cysteine-modified Au-Ag core-shell nanorods. *Sens. Actuators B* 255, 2927–2935. <https://doi.org/10.1016/j.snb.2017.09.113>.
 45. Li, D., Zhang, X., Liu, D., and Wang, T. (2020). Aggregation of non-fullerene acceptors in organic solar cells. *J. Mater. Chem. A* 8, 15607–15619. <https://doi.org/10.1039/d0ta03703f>.
 46. Noriega, R., Rivnay, J., Vandewal, K., Koch, F.P.V., Stingelin, N., Smith, P., Toney, M.F., and Salleo, A. (2013). A general relationship between disorder, aggregation and charge transport in conjugated polymers. *Nat. Mater.* 12, 1038–1044. <https://doi.org/10.1038/nmat3722>.
 47. Marina, S., Gutierrez-Fernandez, E., Gutierrez, J., Gobbi, M., Ramos, N., Solano, E., Rech, J., You, W., Hueso, L., Terçjak, A., et al. (2022). Semi-paracrystallinity in semi-conducting polymers. *Mater. Horiz.* 9, 1196–1206.
 48. Li, S., Ye, L., Zhao, W., Zhang, S., Mukherjee, S., Ade, H., and Hou, J. (2016). Energy-level modulation of small-molecule electron acceptors to achieve over 12% efficiency in polymer solar cells. *Adv. Mater.* 28, 9423–9429. <https://doi.org/10.1002/adma.201602776>.
 49. Zhao, W., Li, S., Yao, H., Zhang, S., Zhang, Y., Yang, B., and Hou, J. (2017). Molecular optimization enables over 13% efficiency in organic solar cells. *J. Am. Chem. Soc.* 139, 7148–7151. <https://doi.org/10.1021/jacs.7b02677>.
 50. Zhang, H., Yao, H., Hou, J., Zhu, J., Zhang, J., Li, W., Yu, R., Gao, B., Zhang, S., and Hou, J. (2018). Over 14% efficiency in organic solar cells enabled by chlorinated nonfullerene small-molecule acceptors. *Adv. Mater.* 30, 1800613. <https://doi.org/10.1002/adma.201800613>.
 51. Fang, J., Liu, Q., Zhang, J., Ye, L., Wu, J., Wei, Z., Guo, X., Zhang, M., and Li, Y. (2020). Efficient as-cast polymer solar cells with high and stabilized fill factor. *Sol. RRL* 4, 2000275. <https://doi.org/10.1002/solr.202000275>.

52. Huang, J., Tang, H., Yan, C., and Li, G. (2021). 1, 1-dicyanomethylene-3-indanone end-cap engineering for fused-ring electron acceptor-based high-performance organic photovoltaics. *Cell Rep. Phys. Sci.* *2*, 100292. <https://doi.org/10.1016/j.xcrp.2020.100292>.
53. Fej, Z., Eisner, F.D., Jiao, X., Azzouzi, M., Röhr, J.A., Han, Y., Shahid, M., Chesman, A.S.R., Easton, C.D., McNeill, C.R., et al. (2018). An alkylated indacenodithieno[3, 2-b]thiophene-Based nonfullerene acceptor with high crystallinity exhibiting single junction solar cell efficiencies greater than 13% with low voltage losses. *Adv. Mater.* *30*, 1800728. <https://doi.org/10.1002/adma.201800728>.
54. Zhang, G., Chen, X.K., Xiao, J., Chow, P.C.Y., Ren, M., Kupgan, G., Jiao, X., Chan, C.C.S., Du, X., Xia, R., et al. (2020). Delocalization of exciton and electron wavefunction in non-fullerene acceptor molecules enables efficient organic solar cells. *Nat. Commun.* *11*, 3943. <https://doi.org/10.1038/s41467-020-17867-1>.
55. Fang, J., Wang, Z., Zhang, J., Zhang, Y., Deng, D., Wang, Z., Lu, K., Ma, W., and Wei, Z. (2015). Understanding the impact of hierarchical nanostructure in ternary organic solar cells. *Adv. Sci.* *2*, 1500250. <https://doi.org/10.1002/adv.201500250>.
56. Zhu, L., Zhang, M., Zhou, G., Hao, T., Xu, J., Wang, J., Qiu, C., Prine, N., Ali, J., Feng, W., et al. (2020). Efficient organic solar cell with 16.88% efficiency enabled by refined acceptor crystallization and morphology with improved charge transfer and transport properties. *Adv. Energy Mater.* *10*, 1904234. <https://doi.org/10.1002/aenm.201904234>.